Supplementary Information (SI) for Journal of Materials Chemistry A.

Robust Nanoporous NiMn oxide Electrocatalysts for Oxygen Evolution Reaction through Defect Engineering

Arpit Thomas[a], Ambrish Kumar[a], Ram K. Sharma[b], Edgar C. Buck[c], Bharat Gwalani[d], Meha Bhogra[a,#], Harpreet Singh Arora[a, #]

[a] Department of Mechanical Engineering, Shiv Nadar Institution of Eminence, Deemed to be University, India (UP)- 201310

[b]Centre for Inter-Disciplinary Research and Innovation, University of Petroleum and Energy Studies, Bidholi Via-Prem Nagar, Dehradun-248007

[c]Pacific Northwest National Laboratory, Richland, Washington99354, United States

[d]Department of Materials Science and Engineering, North Carolina State University, Raleigh, North Carolina 27695, United States

[#]Corresponding author's E-mail: harpreet.arora@snu.edu.in; meha.bhogra@snu.edu.in

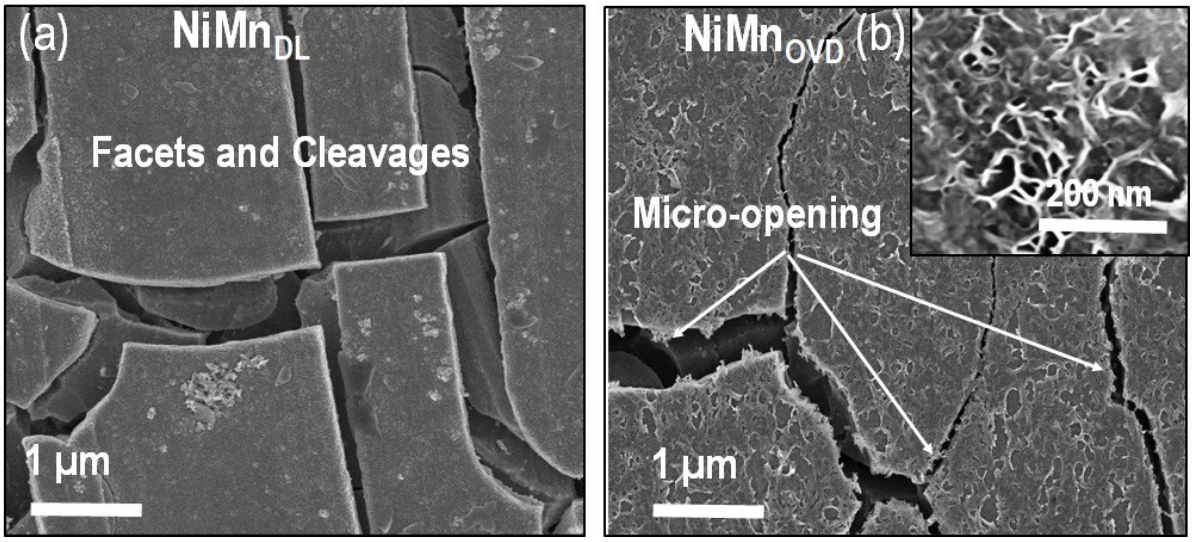

Figure S1: Scanning electron microscope (SEM) images of (a) NM_{DL}, and (b) NM_{OVD}.

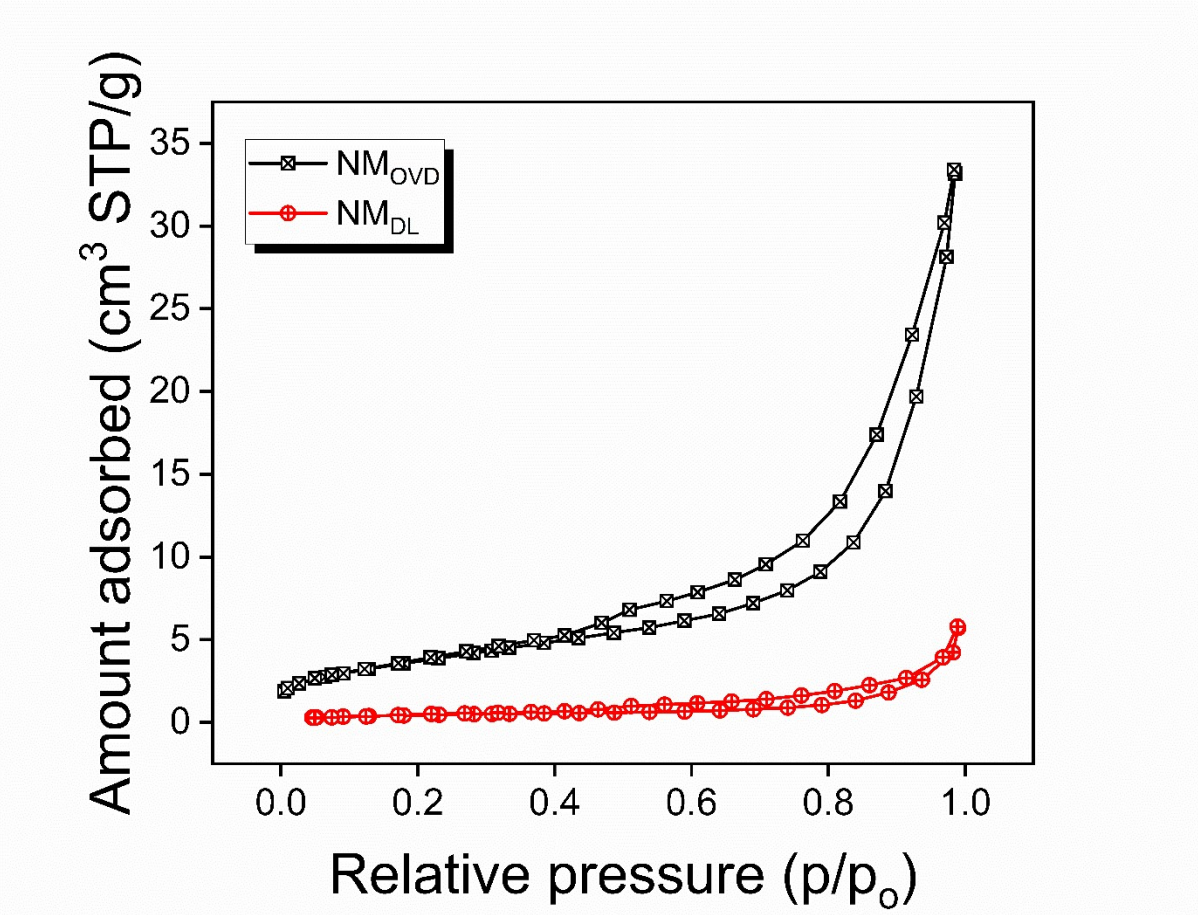

Figure S2: BET analysis for NM_{OVD} and NM_{DL} samples.

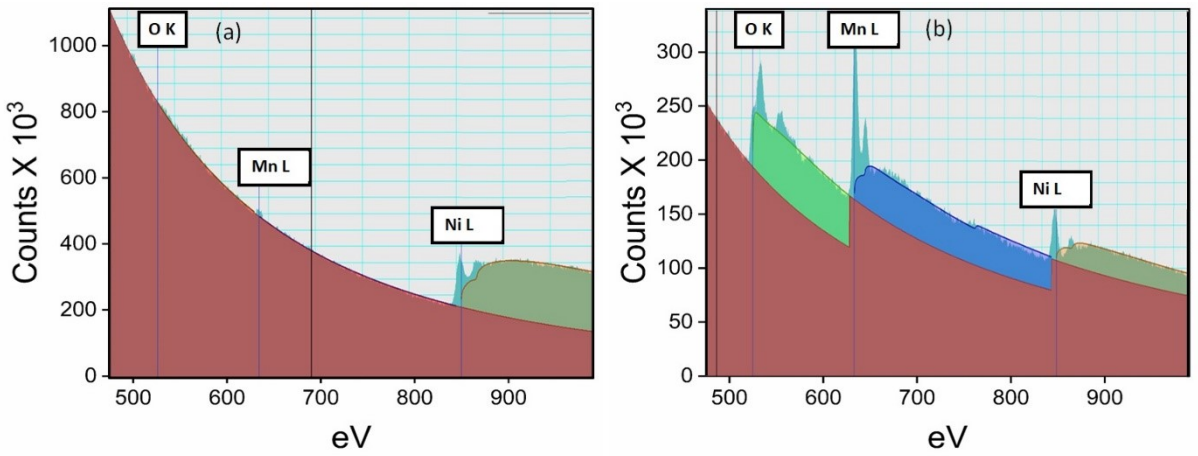

Figure S3: Electron energy loss spectroscopy (EELS) analysis- counts vs binding energy (a) for pure Nickel; (b) for $NiMnO_3$ Phase

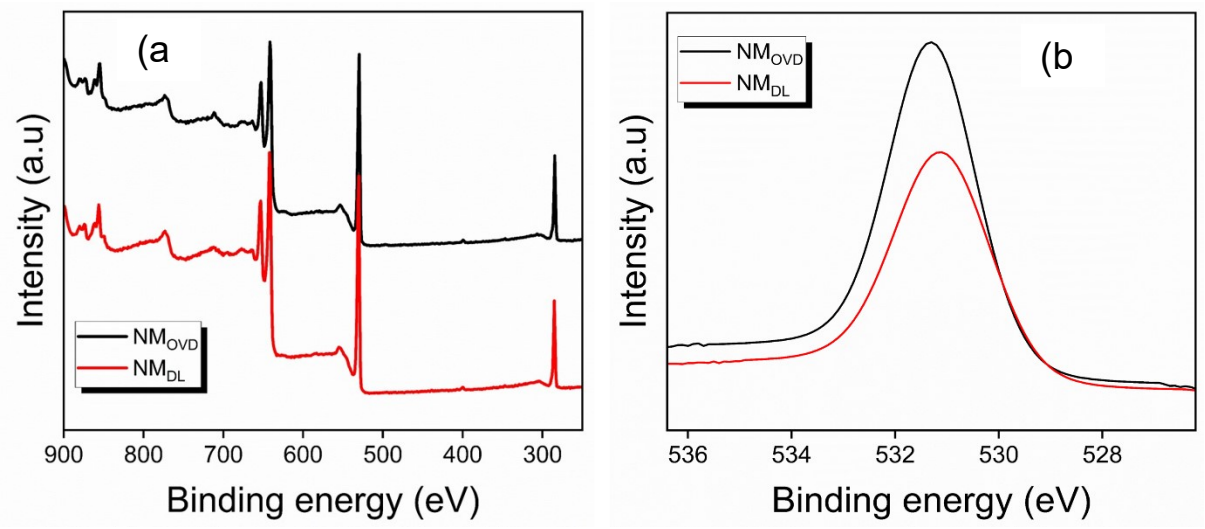

Figure S4: (a) XPS survey scan for as-synthesized pristine dealloyed (NM_{DL}) and deformed dealloyed (NM_{OVD}) specimen, (b) Comparison of oxygen vacancy peak for NM_{OVD} and NM_{DL} specimen

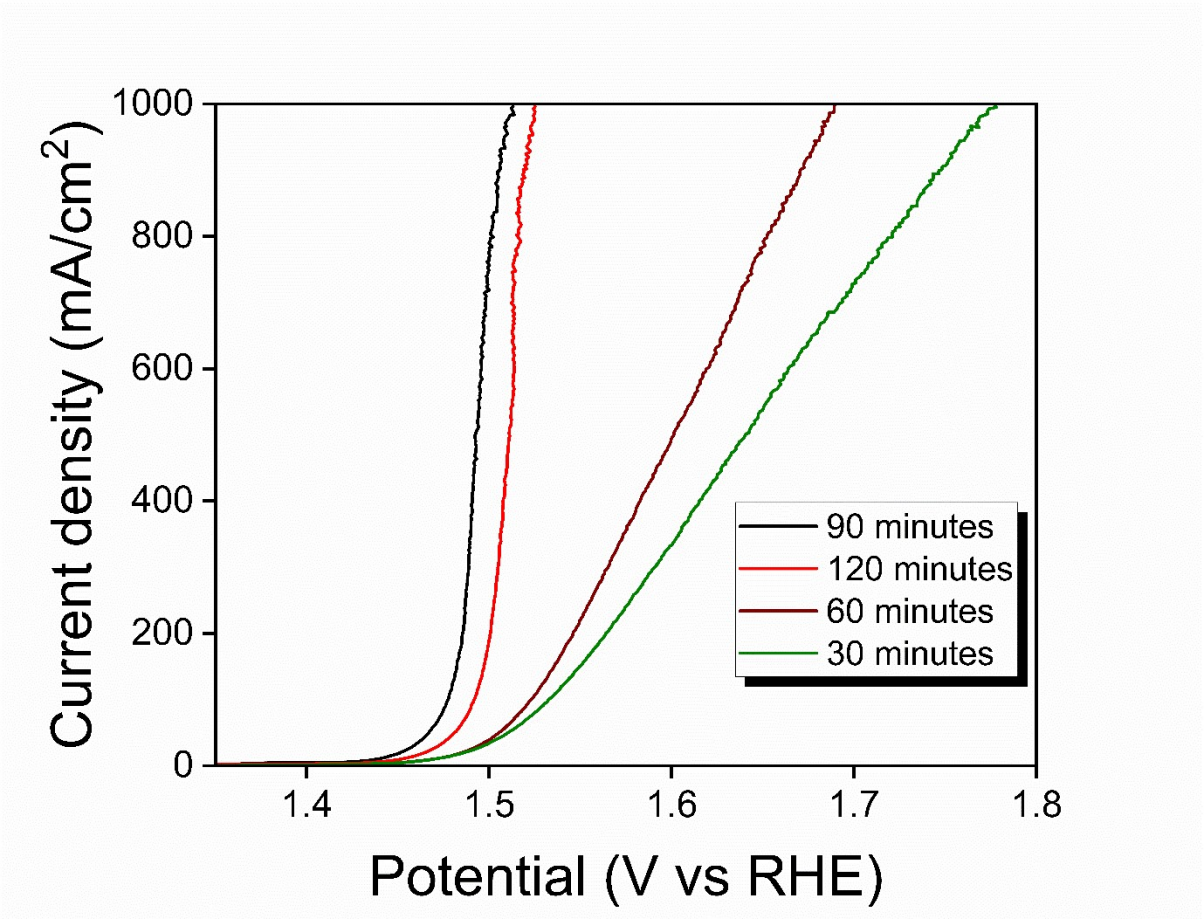

Figure S5: Linear sweep voltammetry curves for NM_{OVD} specimen, dealloyed for different time intervals.

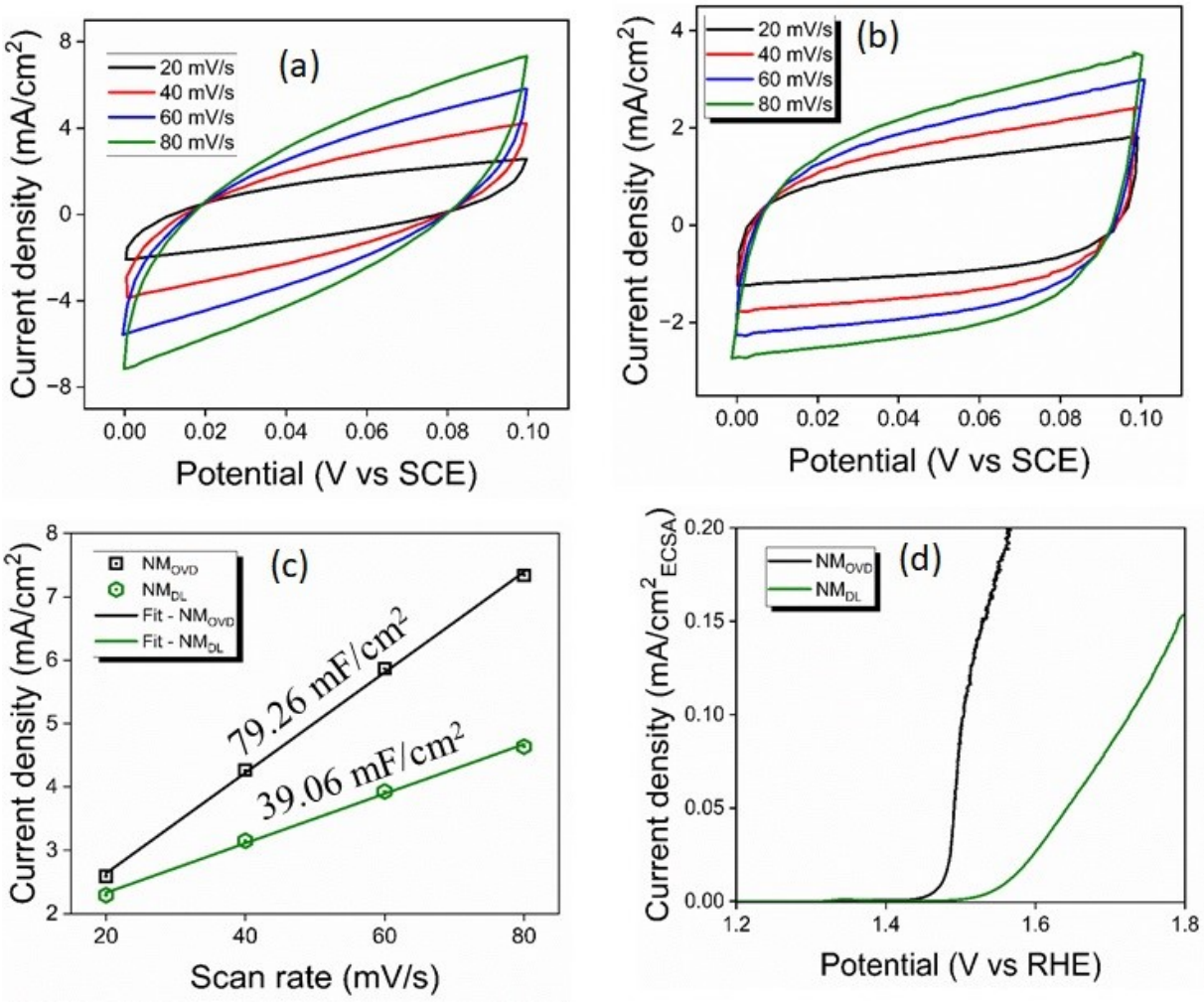

Figure S6: Cyclic voltammetry curves in the non-faradaic region for (a) NM_{OVD}, (b) NM_{DL}, (c) double layer capacitance (C_{dl}) from cyclic voltammetry response, (d) electrochemical active surface area (ECSA) normalized LSV curves for NM_{OVD} and NM_{DL}.

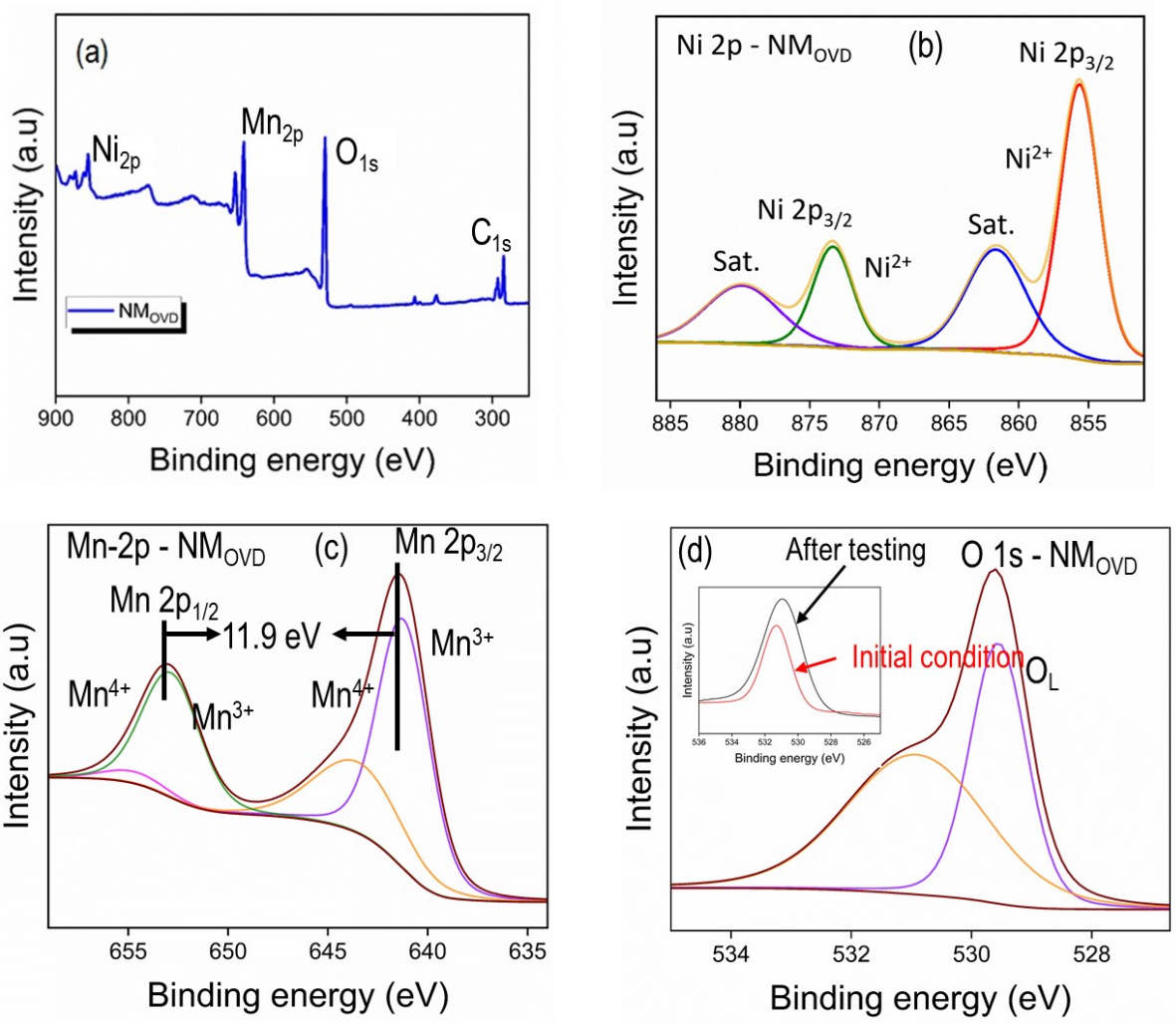

Figure S7: (a) XPS survey scan for NM_{OVD} after chronopotentiometry at 500 mA/cm^2 for 24 hours; (b)-(d) high resolution XPS spectra of Ni2p, Mn2p and O1s for NM_{OVD} specimen after 24 hour chronopotentiometry test at 500 mA/cm^2. Inset of (d) shows the comparison of O1s peak before and after OER testing.

Computational details: Our calculations are based on first-principles density functional theory (DFT) and spin-polarized plane-wave pseudopotential method as implemented in Vienna Ab Initio Simulation Package (VASP)[1, 2]. The ionic core−valence electron interactions are represented with Projector augmented wave (PAW) potentials[3] and electronic exchange−correlation energy is approximated with a generalized gradient approximation (GGA) as parameterized by Perdew−Burke−Ernzerhof[4]. As transition-metal oxides are strongly-correlated systems, the short-range interactions between electrons and electron-localization effects are accounted for by adding Hubbard *U* terms. We use rotationally invariant approach to DFT+U, introduced by Dudarev et al.[5] with U = 1.0 and 6.0 eV for Mn and Ni in $NiMnO_3$ and U = 2.5 and 3.5 eV for Mn^{2+} and Mn^{3+} species in Mn_3O_4. The parameters are determined self-consistently to match the electronic band gap and magnetic moments of elements as determined experimentally in the earlier literature. Kohn−Sham wave functions are expanded in a plane-wave basis set truncated with an energy cut-off of 450 eV. Integrations over Brillouin Zone (BZ) are sampled with a uniform (4 4 4) and (2 2 1) **k**-grid for Mn_3O_4 and $NiMnO_3$ bulk structures respectively, and the atomic structures are relaxed using Broyden, Fetcher, Goldfarb, Shanno (BFGS)-based algorithm until the Hellman−Feynman forces on each atom are lower than 0.01 eV/Angstrom. The transition states (TSs) are obtained using the climbing-image nudged elastic band (NEB) method[6]. Four intermediate images are used in all the NEB calculations. All intermediate images are relaxed until the Hellman−Feynman forces on each atom are within 0.03 eV/Angstrom.

Nature of OER on $NiMnO_3$ in high-coverage regime

To further determine how the LOM mechanism proceeds in the presence of surrounding OH ions in the medium (high-coverage regime), we added OH group in the neighborhood of O_L-O bond (in Figure 6(d)). On energy minimization, the optimized structure shows the formation of *OOH, *OH, H_2O species, along with the O_2 formation (Figure 6(i,j)). Evidently, the chemical interactions of the OH ions and the surface can result in cleaved Ni-O bonds (Figure 6(i)) or dipolar interactions allowing electronic charge transfer between adsorbed species over the $NiMnO_3$ surface (Figure 6(j)). The latter stems primarily from the high electronegativities of O_L of Mn-O_L-Ni and Mn-O_L sites, which bond strongly with H ion of the OH groups, hence releasing O-O molecules[7]. The broken Ni-O bond re-forms itself in this process (Figure 6(j)), highlighting the cyclic and self-propagating nature of the OER process on $NiMnO_3$ surface. This reinforces the prevalence of multi-site OER mechanisms, like LOM, in $NiMnO_3$ over the AEM mechanism prevalent in most transition metal-oxides.

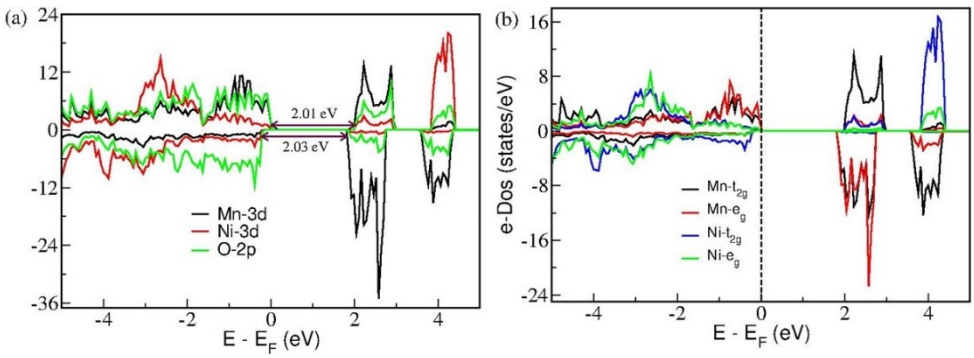

Figure S8: Electronic structure of bulk NiMnO3, (a) showing a semi-metallic nature with a band gap of ~2.0 eV, with prevalence of Mn-3d and O-2p states at the valence band maximum crossing Fermi level, (b) higher density of occupied Mn-e_g orbitals than Mn-t_{2g}, suggesting crucial role of Mn in catalytic performance of $NiMNO_3$

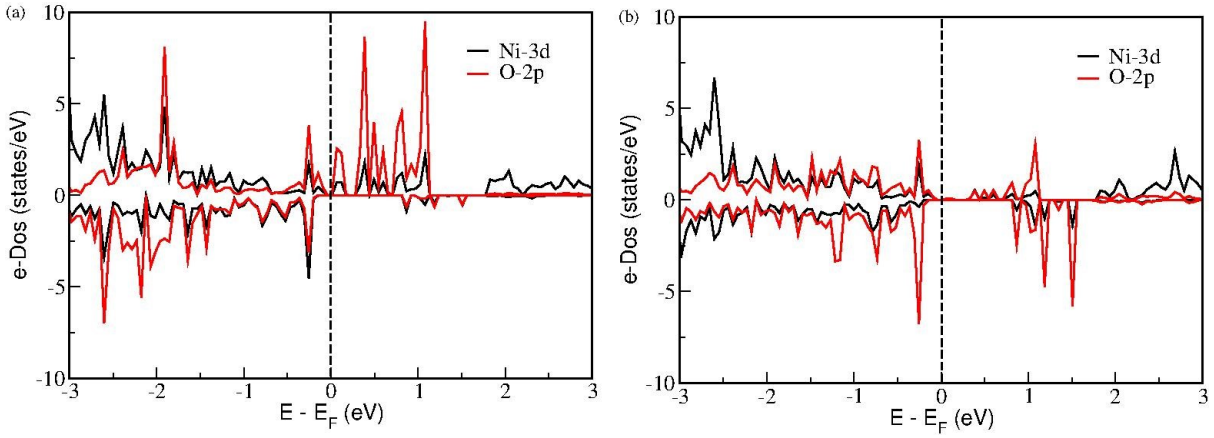

Figure S9: Electronic structures of distinct Ni atoms on the (001) surface; (a) Ni atoms with dangling Ni-O bonds (dark blue), and (b) Ni with Ni-Mn-Ni coordinated O atoms (cyan). The former shows an absence of band gap, with high density of O-2p states, signifying electronic charge transfer from O- to Ni. This Ni-O bond cleaves readily and lead to direct evolution of O_2 through LOM mechanism.

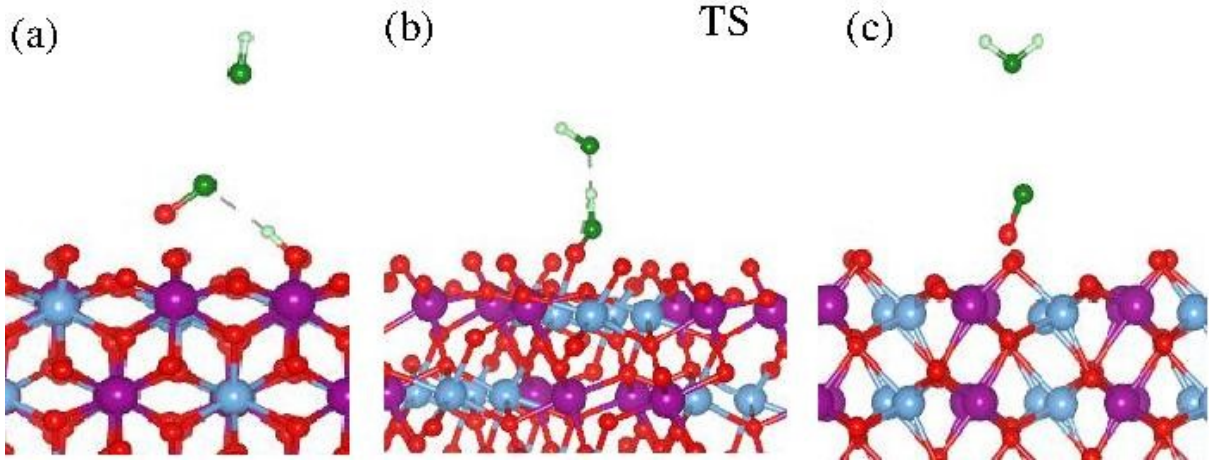

Figure S10. Transition state for the reaction intermediate *OH → *O on pristine $NiMnO_3$ surface: (a) starting configuration, DE = 0 eV, (b) transition state, showing formation of H bonds between two OH groups, DE = 0.37 eV, and (c) release of water molecule and resulting deprotonation of OH group, DE = -1.1 eV.

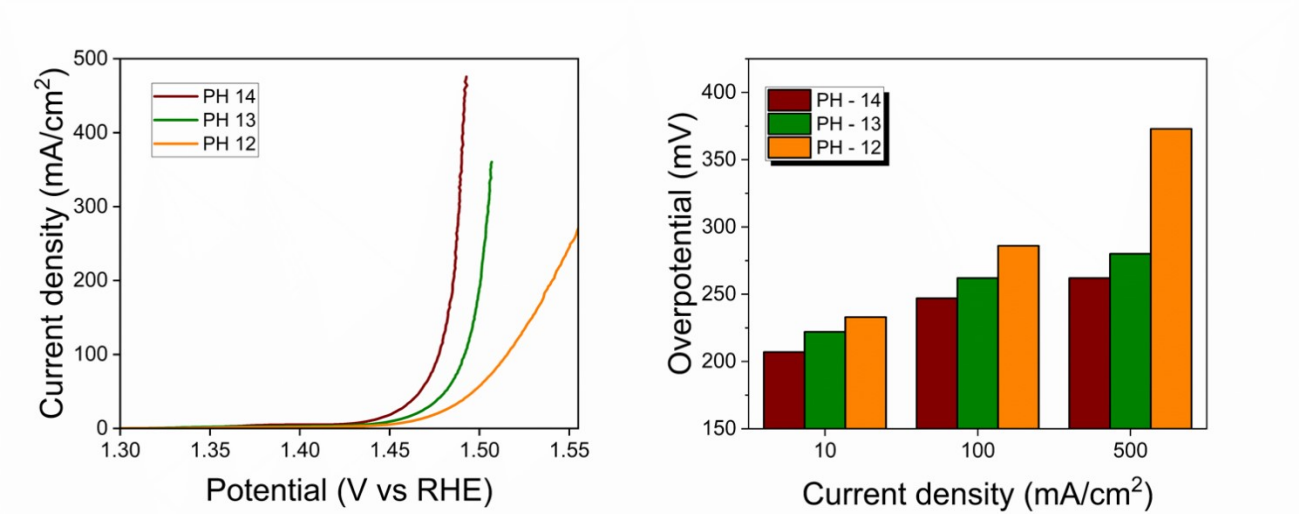

Figure S11: OER activity as a function of pH

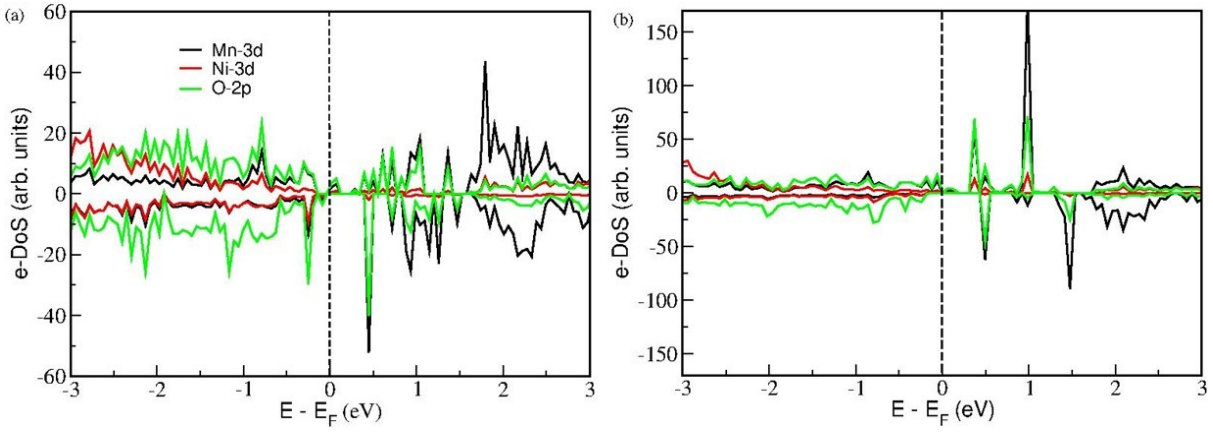

Figure S12: Electronic structure of two different vacancy configurations; (a) very low formation-energy configuration involving cleavage of Ni-O bond, and (b) structure involving structural re-construction and formation of Ni-O and Mn-O distorted polyhedra. The e-DoS of latter shows a sharp increase in Mn-3d states in conduction bands signifying enhanced oxidation kinetics of adsorbates.

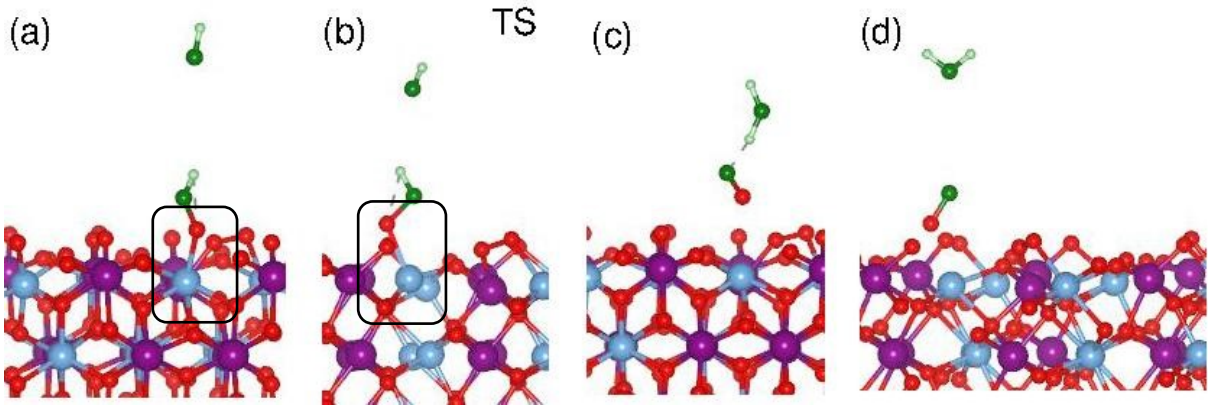

Figure S13. Transition state for the reaction intermediate *OH → *O on $NiMnO_3$ surface containing O vacancy: (a) starting configuration, DE = 0 eV, (b) transition state, showing long-ranged interaction of OH group with adsorbed OH, resulting in the elongation of Ni-O bond from 1.92 Å to 2.06 Å, signifying cleavage of Ni-O bond and activation of LOM mechanism, DE = 1.32 eV, (c) formation of O_L-O group and H_2O molecule, showing formation of hydrogen bonds, DE = -1.36 eV, and (d) release of water molecule, DE = -2.2 eV.

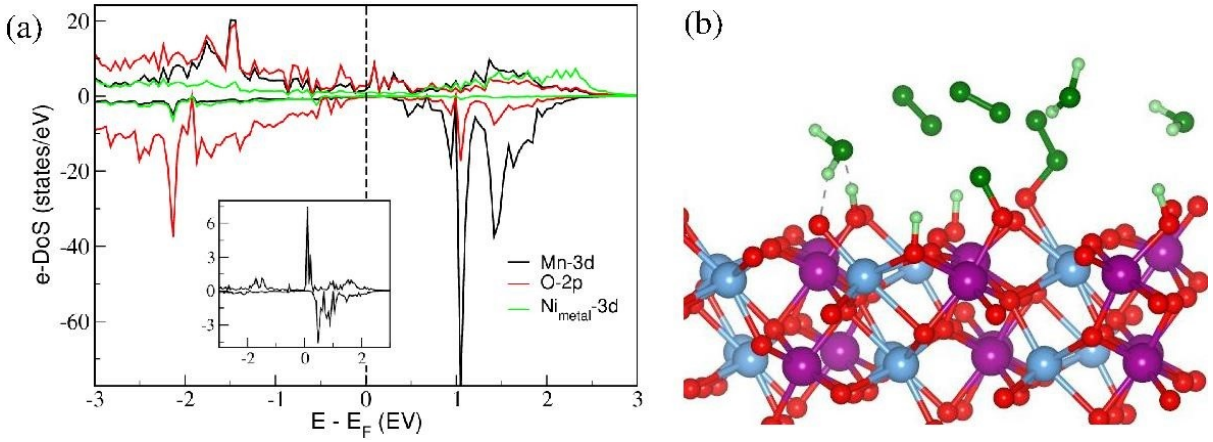

Figure S14: Electronic density of Mn-3d, Ni-3d and O-2p states at the Ni/NiMnO3 junction, showing increase in the density of Mn-3d states in conduction bands. The inset shows the e-Dos of under-coordinated Mn at the interface, showing a sharp increase in density of states at the Fermi-level and in conduction band, strongly indicating its role in OER activity of Ni/NiMnO3 interfaces, (b) direct O_2 evolution from OH group adsorbed in the neighbourhood of Mn-O-O* site, due to H adsorption on electronegative O atoms and resulting cleavage of O-H groups.

Table S1: Comparison of electro-catalytic OER performance of the NM_{OVD} and other self-supported electrocatalysts in 1 M KOH electrolyte. The η_x corresponds to the overpotential at the current density of *x* mA cm^{-2}.

Catalyst	Overpotential (mV)		Ref.
	η_{500}	η_{1000}	
NM_{OVD}	**262**	**282**	**Present Work**
NiFe/NiFe-OH	296	-	Appl. Catal. B: 2020, 278, 119326
NiFe LDH/FeS	304	-	Adv. Funct. Mater. 2019, 29, 1902180
NiFeOOH/NiFe/Ni	290	300	Appl. Surf. Sci 2021, 564, 150440
NiCoV-LTH	340	-	ACS Sustain. Chem. Eng. 2020,8, 16091-16096
NiCe@NiFe/NF-N	-	359	Appl. Catal. B: 2020, 260,118199
Ni-Fe-OH@Ni_3S_2/NF	370	-	Adv. Mater. 2017, 1700404
Fe-NiMo-NH3/H2	244	-	Adv. Energy Mater. 2020, 10, 2002285
Fe,V-Ni_3S_2/NF	-	370	Int. J. Hydrog. Energy, 2022, 47, 14422-14431
Fe-CoP/NF	295	-	Adv. Sci. 2018, 5, 1800949
Cu@NiFe-LDH	311	-	Energy Environ. Sci., 2017, 00, 1-3
FeOOH(Zn-$Fe_xNi_{(1-x)}$OOH	-	330	Small, 2022, 18(37), 2203710
3D Fe^0- Ni_xSy/NF	306	-	ChemElectroChem 2018, 5, 3866-3872
3D	340	-	J. Mater. Chem. A,

Fe2O3@Ni2P/Ni(PO3)2			2019, 7, 965-971
IrNi-FeNi3	300	-	Appl. Catal. B: 2021, 286, 119881
Fe-Ir	300		Appl. Catal. B: 2020, 278, 119327
NCS@CFM-LDH/NF	295	332	Appl. Catal. B: 2022, 121917
NiFeOOH/NiFe/Ni	290	-	Appl. Surf. Sci. 2021, 564, 150440
NiFeOOH(Se)	348	-	J. Am. Chem. Soc. 2019, 141, 7005
Trimetallic MOFs	-	284	Appl. Catal. B: 2020, 119375
NiFeMn/NiFeMn	360	-	Energy Environ. Sci. 2016, 9, 540
Ni@NiFeLDH	349	-	J. Mater. Chem. A, 2019, 7, 21722
CoMoSx	442	-	Angew. Chem. Int. Ed. Engl. 2019, 59, 1659

1. G. Kresse and J. Furthmüller, *Computational materials science*, 1996, **6**, 15-50.
2. G. Kresse and J. Furthmüller, *Physical review B*, 1996, **54**, 11169.
3. P. E. Blöchl, *Physical review B*, 1994, **50**, 17953.
4. J. P. Perdew, K. Burke and M. Ernzerhof, *Physical review letters*, 1996, **77**, 3865.
5. S. L. Dudarev, G. A. Botton, S. Y. Savrasov, C. Humphreys and A. P. Sutton, *Physical Review B*, 1998, **57**, 1505.
6. G. Henkelman, B. P. Uberuaga and H. Jónsson, *The Journal of chemical physics*, 2000, **113**, 9901-9904.
7. A. Zagalskaya and V. Alexandrov, *ACS Catalysis*, 2020, **10**, 3650-3657.